

Two generations of exsolution lamellae in pyroxene from Asuka 09545: Clues to the thermal evolution of silicates in mesosiderite

Pittarello, Lidia; Seann, McKibbin; Akira, Yamaguchi; Gang, Ji; Dominique, Schryvers; Vinciane, Debaille; Claeys, Philippe

Published in:
American Mineralogist

DOI:
[10.2138/am-2019-7001](https://doi.org/10.2138/am-2019-7001)

Publication date:
2019

License:
Unspecified

Document Version:
Accepted author manuscript

[Link to publication](#)

Citation for published version (APA):

Pittarello, L., Seann, M., Akira, Y., Gang, J., Dominique, S., Vinciane, D., & Claeys, P. (2019). Two generations of exsolution lamellae in pyroxene from Asuka 09545: Clues to the thermal evolution of silicates in mesosiderite: American Mineralogist. *American Mineralogist*, 104(11), 1663-1672. <https://doi.org/10.2138/am-2019-7001>

Copyright

No part of this publication may be reproduced or transmitted in any form, without the prior written permission of the author(s) or other rights holders to whom publication rights have been transferred, unless permitted by a license attached to the publication (a Creative Commons license or other), or unless exceptions to copyright law apply.

Take down policy

If you believe that this document infringes your copyright or other rights, please contact openaccess@vub.be, with details of the nature of the infringement. We will investigate the claim and if justified, we will take the appropriate steps.

Two generations of exsolution lamellae in pyroxene from Asuka 09545: clues to the thermal evolution of silicates in mesosiderite.

Lidia PITTARELLO*^{1,2}, Seann McKIBBIN^{1,3}, Akira YAMAGUCHI⁴, Gang Ji^{5,6},
Dominique SCHRYVERS⁵, Vinciane DEBAILLE⁷, Philippe CLAEYS¹

¹Analytical, Environmental, and Geo-Chemistry (AMGC), Vrije Universiteit Brussel,
Pleinlaan 2, B-1050 Brussels, Belgium

²Present address: Department of Lithospheric Research, University of Vienna,
Althanstraße 14, A-1090 Vienna, Austria (lidia.pittarello@univie.ac.at)

³Present addresses: Institut für Geowissenschaften, Universität Potsdam, Haus 27, Karl-
Liebknecht-Straße 24-25, 14476 Potsdam-Golm, Germany, and Geowissenschaftliches
Zentrum, Georg-August Universität, Goldschmidtstraße 1, 37073 Göttingen, Germany

⁴National Institute of Polar Research, Antarctic Meteorite Research Center, 10-3
Midoricho, Tachikawa, Japan

⁵Electron Microscopy for Materials Science (EMAT), University of Antwerp,
Groenenborgerlaan 171, B-2020 Antwerp, Belgium

⁶Present address: Unité Matériaux et Transformations, CNRS UMR 8207, Université de
Lille, Villeneuve d'Ascq, 59655 France

⁷Laboratoire G-Time (Géochimie: Traçage isotopique, minéralogique et élémentaire),
Université Libre de Bruxelles, Av. F.D. Roosevelt 50, 1050 Brussels, Belgium B-1050
Brussels, Belgium

Abstract

Mesosiderite meteorites consist of a mixture of crustal basaltic or gabbroic material and metal, possibly derived from the same planetesimal parent body, and their formation process is still debated due to their unexpected combination of crust and core materials while lacking an intervening mantle component. Mesosiderites have experienced an extremely slow cooling rate from ca. 550°C, as recorded in the metal (0.25-0.5°C/Ma). Here we present a detailed investigation of exsolution features in a monoclinic low-Ca pyroxene from the Antarctic mesosiderite Asuka (A) 09545. Two generations of exsolution lamellae are present, with lamellae 1 consisting of augite blebs and lamellae 2, within lamellae 1, of clinoenstatite. Geothermobarometry calculations, lattice parameters, lamellae orientation, and the inversion to clinoenstatite were used in an attempt to constrain the history and cooling rate of pyroxene from 1150°C to 570°C. The formation of two generations of exsolution lamellae requires relatively slow cooling and the preservation of such fine-grained lamellae limits reheating to a peak temperature lower than 570°C. These features, including the presence of monoclinic low-Ca pyroxene as host, are exhibited by only a few mesosiderites, suggesting a different origin and different thermal history from most mesosiderites and that the crystallography (i.e. space group) of low-Ca pyroxene could be a diagnostic cooling rate indicator for this class of meteorites.

Keywords: pyroxene, exsolution, mesosiderite, thermal history, cooling rate

44

45

Introduction

46

Mesosiderites are stony-iron meteorites that consist of a breccia containing roughly equal amounts of metal and silicate (e.g., Prior, 1918; Rubin and Mittlefehldt, 1993). The metal component shows some similarities to IIIAB iron meteorites (Hassanzadeh, et al., 1990), whereas the silicate fraction has been compared with basaltic or pyroxenitic Howardite-Eucrite-Diogenite (HED) meteorites (e.g., Clayton and Mayeda, 1996; Greenwood et al., 2015), although they likely originated in a different parent body than the probable source for most of the HED meteorites, the asteroid 4-Vesta (Rubin and Mittlefehldt, 1993). The simultaneous presence of silicate and metal is interpreted as a mixture of basaltic material from the crust and metal from the core, originating either by collision of two differentiated parent bodies (Wasson and Rubin 1985) or from mixing within the same parent body (Mittlefehldt et al., 1998; Scott et al., 2001). The silicate fraction generally consists of basaltic to cumulate gabbro and pyroxenitic clasts, locally including olivine nodules exhibiting thick reaction rims (e.g., Ruzicka et al. 1994).

59

Mesosiderites are classified on the basis of their internal structure and relative abundance of plagioclase and pyroxenitic phases (Powell 1971; Floran 1978). The most peculiar characteristic of mesosiderites is that the metal has recorded the slowest cooling rate from ca. 550°C ever measured in the Solar System (e.g., Powell, 1969; Kulpecz and Ewins, 1978; Haack et al., 1996; Goldstein et al., 2014).

64

The formation processes of mesosiderites are still debated, and since Prior (1918) many different models have been proposed, involving planetary differentiation (Delaney, 1983), collision with a metal projectile (Wasson and Rubin, 1985), and remelting of

66

67 mixed basalt-gabbro and metal close to the parent body surface (Mittlefehldt, 1990). The
68 currently most credited formation model (e.g., Rubin and Mittlefehldt, 1993; Scott et al.,
69 2001) hypothesizes accretion, followed by different crustal melting phases between 4.56
70 Ga and 4.47 Ga, collisional disruption and gravitational reassembly (3.9 Ga), and finally
71 impact excavation and ejection of buried material. Mixing of metal and crustal silicate
72 should have occurred during one of the crustal remelting phases. This model provides an
73 explanation for the mixture of crustal and core material and for the slow cooling of metal
74 due to deep burial of the mixed material, but still fails to fully explain why no
75 mesosiderites have been found bearing olivine-rich silicate fractions or rapidly cooled
76 metal (Hewins, 1983). However, the thermal history of the mesosiderite parent body is
77 well constrained. After the mixing event (ca. 4.4 Ga), likely of cold silicate with molten
78 metal, mesosiderites experienced fast cooling to ~600°C, subsequent deep burial in the
79 regolith and extremely slow cooling below 600°C (Stewart et al., 1994; Haack et al.,
80 1996). A similar history has been constrained by Sm-Nd geochronology (Stewart et al.
81 1994). The young Ar-Ar ages, which were previously interpreted as an impact-induced
82 resetting at 3.9 Ga (Bogard et al., 1990), might simply be caused by the extremely slow
83 cooling of the mesosiderites through the closure temperature for Ar diffusion (Bogard
84 and Garrison, 1998). Haba et al. (2017) dated a younger event in zircon than the common
85 formation age, suggesting that this high temperature event could be either the age of
86 mixing between metal and silicate or a large collision that reheated the whole body. An
87 internal formation hypothesis was proposed by Delaney (1983), but rejected by later
88 studies (e.g., Hewins, 1983). In the Earth, the delivery of subducted oceanic basaltic
89 crust to the core-mantle boundary (van der Hilst and Karason, 1999; Andraut et al.,

2014) might lend some inspiration to an internal formation process for mesosiderites, through internal convection in planetesimals (Tkalcic et al., 2013), despite the many differences between Earth and the mesosiderite parent body.

The cooling history of the silicate fraction in mesosiderites is not yet clear. Bogard et al. (1990) summarized the three possible scenarios that are consistent with the radiometric ages: after the formation or reheating up to 1150°C at 4.5 Ga, silicates underwent a) rapid cooling, followed by slow cooling of the metal, b) slow cooling, c) further reheating event at ca. 4 Ga, followed by rapid cooling of silicates down to 550°C and subsequent slow cooling of the metal. Bogard et al. (1990) proposed a fourth scenario, where metal silicate mixing occurred at 4.5 Ga, but an important reheating event (temperature peak lower than 550°C) occurred later at <4 Ga. The estimated peak temperature would have been sufficient to reset the Ar age, but not to affect the silicates. Most estimates agree that the silicate cooling rate was fast until ca. 800°C (Delaney, 1983; Ruzicka et al., 1994; Ganguly et al., 1994; Stewart et al., 1994), with proposed values of 1-100°C/day (based on pyroxene overgrowth; Delaney, 1981), and 14°C/ka at 1150°C, ca. 5°C/ka at 600°C, and 1°C/Ma at 250°C (based on new data on Fe-Mg diffusion in pyroxene; Ganguly et al., 1994).

In this work, we present a study of mesosiderite Asuka (A) 09545, collected in Antarctica during a joint Belgian-Japanese mission, focusing on pyroxene to characterize the peculiar exsolution processes and constrain the cooling history of silicates in this sample. By comparison with other mesosiderites in the literature, the implications of such observations on the formation processes of mesosiderites are discussed.

Methods

A polished thin section (thickness 35 μm) and a thick polished chip of sample A 09545 were investigated in this work (Fig. 1a). Scanning electron microscopy (SEM) has been performed at the Royal Belgian Institute of Natural Science (RBINS), Brussels, Belgium, with a FEI Inspect S50 instrument, equipped with an energy-dispersive spectrometry (EDS) detector, and at the Vrije Universiteit Brussel, Brussels, Belgium, with a JEOL 6400 SEM. Experimental conditions were 10 mm of minimum working distance, 15 kV acceleration voltage, ca. 300 pA beam current, and 4–6 μm of spot size. Quantitative analysis of the composition of the investigated phases has been evaluated with a JEOL JXA-8200 electron microprobe, equipped with five wavelength-dispersive spectrometers (WDS) and one EDS, at the National Institute of Polar Research (NIPR), Tachikawa, Japan. Operative conditions were 15 kV acceleration voltage, 12 nA beam current, and with a fully focused beam. The ZAF corrections were applied. Detection limit for major elements are: 130 $\mu\text{g/g}$ for Si, 140 $\mu\text{g/g}$ for Ti, 90 $\mu\text{g/g}$ for Al, 170 $\mu\text{g/g}$ for Cr, 230 $\mu\text{g/g}$ for Fe, 240 $\mu\text{g/g}$ for Mn, 60 $\mu\text{g/g}$ for Mg, 60 $\mu\text{g/g}$ for Ca, 110 $\mu\text{g/g}$ for Na, and 100 $\mu\text{g/g}$ for K. Natural and synthetic materials obtained from C.M. Taylor Company were used as mineral reference materials. The composition of pyroxene is expressed as end member components: enstatite (En) mol%, ferrosilite (Fs) mol%, and wollastonite (Wo) mol%. Image analysis for quantitative petrography has been applied on BSE-SEM images, using the free software ImageJ.

A FEI Helios NanoLab 650 dual beam system (Field Emission-FE-SEM and focused ion beam-FIB) was used to prepare site-specific transmission electron microscopy (TEM) samples by Ga^+ ion sputtering, with an ion beam accelerating voltage of 30 kV and a

beam current of 3 nA. TEM has been performed with a Philips CM20 instrument, operated at 200 kV and equipped with a Nanomegas “Spinning Star” precession unit and an Oxford INCA x-sight EDS detector. Microdiffraction, i.e., with a nearly parallel incident beam focused on the specimen with a spot size in the range 10-50 nm, was performed to acquire a single-crystal zone-axis pattern (ZAP). The precession semi-angle was set to 2° to significantly reduce overall dynamical effects. Java electron microscopy simulator (JEMS) software was used for simulation of electron diffraction patterns assuming a kinematic approximation (Stadelmann 2004). Both instruments are located at the Electron Microscopy for Materials Science (EMAT) laboratory of the University of Antwerp, Belgium. Additional optical microscopy was performed at the Natural History Museum of Vienna, Austria, on selected thin sections of mesosiderites from the local collection.

Results

Petrographic, geochemical, and crystallographic observations

The sections obtained from A 09545 consist of a clast-supported breccia, with gabbroic clasts of various sizes, containing pyroxene and plagioclase, and amoeboid metal (Fig. 1). The metal fraction is 20-30% in volume, as calculated by image analysis on BSE-SEM images. The sample is crosscut by veins with products of alteration and oxidation, due to terrestrial weathering. No olivine has been detected in this fragment. However, a large nodule with an olivine core and a corona mantle has detached from the sample during the preparation and has been included in the polished chip. In this work, this nodule will not be considered. Plagioclase is anorthitic (An₉₁) and has a homogeneous

composition throughout the sample. Silicate clasts contain also chromite, apatite, and a minor amount of free silica, the latter mostly localized in the upper corner of the polished chip (Fig. 1).

According to the mineralogic classification of the silicate fraction (Mittlefehldt et al. 1998), the sample belongs to the compositional class B mesosiderites, due to the high amount of low-Ca pyroxene with respect to plagioclase, ca. 75% to 25%, respectively, as determined by image analysis on BSE-SEM images (class A are more "basaltic" rather than "pyroxenitic", with near equal proportions of plagioclase and pyroxene). The lack of clastic matrix suggests complete recrystallization, a relatively high metamorphic grade, and textural classification of type 3 (Powell 1971; Floran 1978). Overall this sample can be considered a cumulate gabbro (Rubin and Mittlefehldt 1992).

Figure 1

Pyroxene in the clasts can reach several hundreds of μm in size. All pyroxene crystals, independently on their size, contain two generations of exsolution lamellae. The pyroxene host (host px) is low-Ca clinopyroxene, with composition $\text{Wo}_3\text{En}_{59}\text{Fs}_{38}$ as determined with the electron microprobe (Table 1), and with a diffraction pattern consistent with monoclinic "ferrosilite", space group $\text{P2}_1/\text{c}$, which can be technically classified as clinoenstatite considering the chemistry (Fig. 2).

Exsolution lamellae 1 (lam 1). The first generation of exsolution lamellae has an orientation roughly parallel to cleavage and is consistent in all lamellae belonging to the same host grain. Lamellae appear in this section as elongated domains with vermicular shape and lower BSE contrast than the host pyroxene. The average size is 20-30 μm in thickness and up to 100 μm in length, depending on the section. The composition of the

lamellae corresponds to augite $\text{Wo}_{42}\text{En}_{41}\text{Fs}_{17}$ (Table 1) and the diffraction pattern to that of monoclinic high-Ca pyroxene (space group C2/c ; Fig. 2).

Exsolution lamellae 2 (lam 2). Lam 1 contains another set of lamellae. Lamellae 2 are organized in subparallel sets, which appear brighter than lam 1 in BSE-SEM images. The thickness is generally lower than 300 nm, with a regular spacing of about 900 nm. The composition of lam 2 roughly corresponds to $\text{Wo}_0\text{En}_{56}\text{Fs}_{43}$, as determined by standardless EDS-TEM measurements (Table 1), and the diffraction pattern is consistent with that of clinoenstatite (space group $\text{P2}_1/\text{c}$). The composition and the crystal symmetry, therefore, are similar to those of the host pyroxene, but in lam 2 Ca appears to be below the detection limit. The orientation of lam 2 has been reestablished to be parallel to $[001]$ (Fig. 3).

Figures 2-3. Table 1

Discussion

Geothermobarometric calculations

The two-pyroxene geothermobarometer of Putirka (2008) and the improved version of Nakamuta et al. (2017), which accounts for the influence of Na, Cr, and Al in the octahedron, have been used to determine the equilibration temperature of the exsolution events. The geothermobarometer of Putirka (2008) was calibrated for the temperature range 950-1400°C, consistent with that experienced by the investigated pyroxene, but for a pressure of ca. 1 GPa, much higher than the assumed pressure recorded by the selected sample, limiting its applicability to determine pressure values. As the first exsolution (inverted pigeonite), resulted in the augite that further exsolved low-Ca pyroxene (lam

2), the original composition of the augite was calculated by evaluating the contribution of the exsolved lam 2 with image analysis (ca. 14% surface; Table 1). The equilibrium conditions between the host and the augite yield a temperature of 946-1028°C and a pressure of ca. 2-24 Kbar following the geothermobarometer of Putirka (2008), and a temperature of 976-1080°C following the geothermometer of Nakamuta et al. (2017). This is roughly consistent with the graphical evaluation based on Lindsley (1983; Fig. 4). The composition of lam2 could be determined only by EDS at the TEM and no Ca was detected. The equilibrium conditions between lam 1 and lam 2 strongly depend on the CaO content in lam 2. Assuming a CaO content of 0.1-0.2 wt% (a reasonable detection limit for the instrument), the equilibration temperature according to the geothermometer by Brey and Kohler (1990) is 681-809°C (only one managed to converge). Following the geothermometer of Nakamuta et al. (2017), the temperature range for the second exsolution is 542-811°C. In any case, the lower content of CaO in the second exsolution process indicates a lower equilibrium temperature than for pigeonite inversion, as also suggested by the graphical evaluation based on the diagram provided by Lindsley (1983; Fig. 4).

Fig. 4

Cooling rate evaluation

Miyamoto and Takeda (1977) determined the cooling rate of eucrites based on the thickness of pyroxene exsolution lamellae. Extrapolating their evaluation to our sample, we obtain a cooling rate of ca. 1°C/Ka for lam 1 and 10°C/yr for lam 2. Grove (1982) used exsolution lamellae in Lunar pyroxene to estimate the cooling rate in the temperature range 1100-800°C. The orientation and the symmetry class of the exsolution

lamellae in pyroxene in the investigated mesosiderite are the same as those in the Lunar samples, as well as the temperature range of formation. Qualitatively extrapolating the evaluation presented in Grove (1982) to our lamellae, we obtained a cooling rate of ca. 10°C/Ma for lam 1, and a faster cooling rate, but slower than the 0.02°C/hr determined for the Lunar pyroxene, for lam 2. However, the thickness of lamellae alone has proven not to be reliable in estimating the cooling rate of pyroxene, because it is potentially controlled also by other factors and different lamella thicknesses can be exhibited in the same sample (e.g., Miyamoto et al. 2001; Sugiura and Kimura 2015).

Additional temperature evaluations based on crystallographic characteristics

The formation of exsolution lamellae at different temperatures has also been related to the angle between the growth direction (considered (001) and (100)) and the c-axis of the host (Robinson et al., 1977). This angle decreases for increasing temperature of formation in the range 850-1050°C. Unfortunately, neither the angle between the lattice directions nor the lattice parameters were determined in A 09545. However, the described features and the lamellae orientation presented by Robinson et al. (1977) match the observations on lam 2 in A 09545. In detail, the deformation features observed in lam 2 (Fig. 3) might have been caused by the speed in changing symmetry class (from C2/c to P2₁/c) that induces lattice strain. The presence of these features and the occurrence of monoclinic, low-Ca pyroxene are consistent with the formation of lam 2 at temperatures in the range 750-900°C.

Nakazawa and Hafner (1977) investigated two generations of exsolution lamellae in pyroxene from Lunar basalt. These authors observed that the crystallographic orientation of lamellae is determined by the crystal symmetry of the original host: lamella along

(001) exsolved from C2/c (high pigeonite) and lamellae along (100) derived from P2₁/c pyroxene. The change in plane of intergrowth depends on the temperature, and in A 09545, the transition between exsolution lamellae subparallel to (100) to those aligned with (001) should have occurred between 550 and 700°C. However, the initial conditions, such as the composition of the pyroxene involved and the overall cooling, in the work by Nakazawa and Hafner (1977) were quite different from those experienced by A 09545, but the presence of (001) lamellae might suggest a similar slow cooling.

Constraining the thermal history of pyroxene from exsolution lamellae

The applicability of the known two-pyroxene geothermometer might be affected by the Ca content in pyroxene (e.g., Bunch and Olsen, 1974) and the Fe content in augite. The latter effect has been recently demonstrated to be negligible (Murri et al., 2016). The effects of Na, Cr, and Al in the octahedron have been taken into account by Nakamuta et al. (2017), updating the geothermometer of Putirka (2008), and resulted to be negligible in our sample. From geothermometric calculations based on the Fe-Mg exchange in pyroxene, together with the other parameters considered in this study (lattice, lamellae orientation, and ortho-clinopyroxene inversion), the cooling of pyroxene can be followed step by step from an initial temperature of 1150°C (crystallization temperature of pigeonite) to ca. 550°C (inversion to clinopyroxene or to low pigeonite), as represented in Fig. 5.

The cooling rate estimated by Ganguly et al. (1994), based on pyroxene zoning in mesosiderite, yielded 1°C/100yr until 850°C and a progressively lower cooling rate for lower temperatures. A more recent study set the change between fast and slow cooling rate at approximately 700°C (Ganguly and Tirone 2001). Our rough calculations indeed

suggest a slower cooling rate at high temperature for the formation of lam 1, but a faster cooling rate at low temperature leading to the formation of lam 2.

A definitive evaluation of the cooling rate in the range 700-550°C would be provided by single crystal diffraction of the host clinoenstatite and of the first generation lamellae (e.g., Molin et al. 2006), following the method of Stimpfl et al. (2015) and Murri et al. (2016), and by modelling in detail the cation exchange (e.g., McCallum et al., 2006). Unfortunately, the presence of inclusions, the grain size, and the accessibility to crushed samples hamper the applicability of this technique to the investigate mesosiderite A 09545.

Numerical modeling demonstrated that slow heating and slow cooling rate is required for pyroxene to register temperature variation (Yamamoto et al., 2017). This excludes impact reheating as the process initiating the exsolution in pyroxene, but rather supports the fact that after initial formation, silicates recorded slow cooling and were not reheated above a certain temperature. Any abrupt reheating above ca. 600°C would have obliterated the described microstructure.

The occurrence of clinoenstatite, rather than orthoenstatite (latter with space group Pbc_a), as host and in lam 2 is further indicative of slow cooling. In most instances of pigeonite inversion, the normal product is a set of augite exsolution lamellae hosted in orthopyroxene. It is possible that in some of the literature the identification of orthopyroxene was based only on the low-Ca content, without pursuing further analyses. According to Ishii and Takeda (1974), exsolution lamellae of augite along (001) form in host metastable pigeonite, whereas augite blebs along (100) form as result of decomposition of pigeonite into orthopyroxene and augite. The different processes are

controlled by the original composition of the pigeonite, which should have been quite Mg-rich to decompose, rather than to exsolve. Although these authors report the presence in the literature of (100) augite blebs in metastable low-Ca pigeonite (called clinohypersthene) in extraterrestrial material, they do not provide a possible explanation of this apparent contradiction to their analyses.

The cooling path of pyroxene in A 09545 likely involved exsolution of high pigeonite (C2/c) hosting augite exsolution lamellae (C2/c), followed by high-low pigeonite transformation (Fig. 5; C2/c to P2₁/c at ~1000 °C; Brown et al. 1972). Such a metastable transformation skips the orthopyroxene field and enables a restructuring of the host high pigeonite crystal into clinoenstatite with only local rearrangement of the lattice. Another possible path would involve decomposition of pigeonite into orthopyroxene and augite blebs upon slow cooling, followed by low temperature transition from orthopyroxene into low-clinopyroxene (Pbca to P2₁/c at 570-600 °C at low pressure; Ulmer and Stalder, 2001, and references therein). However, the transformation of the entire host pyroxene from ortho- into clinoenstatite requires complete restructuring of the crystal (Smith 1969; Ashworth 1980). The exsolution of lam 2 from lam 1 likely proceeded at low temperature and very slow cooling rates, yielding low temperature clinopyroxene (P2₁/c) with very low CaO contents (Fig. 5).

Fig. 5.

Occurrence of exsolution lamellae in pyroxene in other mesosiderite samples.

Exsolution lamellae due to inverted pigeonite have been commonly observed in eucrites and this feature has been interpreted as indicative of slow cooling after a reheating event > 1000°C (e.g., Yamaguchi et al. 1996). Exsolution lamellae resulting from pigeonite

inversion have been described also in a few mesosiderites (e.g., in Alan Hills A77219, Agosto et al. 1980; in Dyarri Island, Lowicz, and Patwar, Delaney et al. 1981, in Estherville, Ganguly et al. 1994; in Morristown and Mount Padbury, Powell 1971; and in Vaca Muerta, Rubin and Jerde 1987), but never investigated in detail. Two generations of exsolution lamellae, similarly to those investigated in this work, were presented by Rubin and Jerde (1987) from the Vaca Muerta mesosiderite. The lithic clasts containing two generations of exsolution lamellae were interpreted by these authors as cumulate eucrite clasts, thermally annealed after incorporation into the mesosiderite. According to Powell (1971), inverted pigeonite with exsolution lamellae along two orientations might be common in the sub-group 3 mesosiderites, including examples such as Lowicz, Mincy, and Morristown. Our study of A 09545 supports this interpretation. In other mesosiderite sub-groups, inverted pigeonite might be present, but only with exsolution along one direction. That the Vaca Muerta mesosiderite, classified as type 1, contains two orientations of exsolution lamellae in some clasts is consistent with a complex multi-stage history for the petrogenesis of this meteorite. Similarly, in some mesosiderites, the exsolution of inverted pigeonite occurs only at the overgrown rim of orthopyroxene (e.g., in Emery and Morristown; Ruzicka et al., 1994).

Other than data from the literature, additional mesosiderites were investigated, as representative of the variety of mesosiderites, from the collection of the Natural History Museum of Vienna, to search for pyroxene internal features. The most common feature observed in pyroxene in mesosiderites is chemical zoning in low-Ca pyroxene, with a rim enriched in Fe with respect to the core of crystals (e.g., in Estherville, Lamont, and Veramin). This feature is commonly attributed to impact reheating followed by relatively

fast cooling and was used to estimate the cooling rate in the range 1150-900°C as 1-100°C/day (e.g., Delaney et al. 1981). Inverted pigeonite is relatively common, but two generations of exsolution lamellae, formed at different temperature during cooling, seems to be rare. However, most of the previous works describe inverted pigeonite as an assemblage of orthopyroxene and augite, without checking by diffraction techniques the real nature of the low-Ca pyroxene. This might actually be clinoenstatite, as in the case of A 09545.

Thermal history of the silicate fraction in the mesosiderite

The silicate fraction of mesosiderites, in particular pyroxene, exhibits a huge variety of internal features. According to Sugiura and Kimura (2015), this variety is due to a range of cooling rates experienced by mesosiderite precursor materials in their parent body after the reheating event. Different burial depths in the parent body might explain these differences. However, this would not be consistent with the model of fast cooling of silicates at high temperature and slow cooling of metal below 700-550°C. This also excludes the possibility that an important reheating event could be invoked, with peak temperature <550°C, because such fine grained features as the two generations of exsolution lamellae in pyroxene observed in A 09545 would have been completely annealed and obliterated. In conclusion, the variety of microstructures exhibited by mesosiderites indicates a complex thermal history that cannot be accommodated by a unique model applicable to the whole collection of mesosiderites. However, our study indicates that microstructural investigations may be able to identify internally consistent subgroups within this class of meteorites using pyroxene crystallography in combination with conventional microprobe chemical compositions.

365

366

Implications

367

The internal features of a mesosiderite, investigated by a classical mineralogical approach, provides important new clues to the thermal history of this sample and the evolution of the mesosiderite parent body(ies). In particular, the crystallography of pyroxene directly correlates with the cooling rate experienced by the material. Among the numerous open questions about mesosiderite formation, the information on the thermal history of its silicate fraction helps constraining several events that affected this class of meteorites.

368

369

370

371

372

373

374

Conclusions

375

Mesosiderites are breccias consisting of a mixture of metal, chemically similar to IIIAB iron meteorites, and silicates, which resemble HED achondrites (Prior, 1918, Powell, 1971). From microscale metallographic textures and geochemistry, the cooling of the metal fraction from about 550°C appears to be uniquely slow (cooling rate of 0.25-0.5°C/My; Goldstein et al., 2014). On the other hand, the silicates are believed to have cooled rapidly, at least until ca. 700°C (e.g., Ganguly et al., 1994). The mesosiderite A 09545 (Yamaguchi et al., 2014) contains coarse-grained low-Ca monoclinic pyroxene that hosts two generations of exsolution lamellae, which can be used to constrain the thermal evolution of the silicate fraction in the sample. Although the exact cooling rate could not be evaluated, the composition, orientation, and lattice parameters of these lamellae suggest a relatively slow cooling from 1150°C to 570°C that can be considered as occurring through several near equilibrium steps (Fig. 6). The occurrence of these features, as well as the unexpected monoclinic crystallography of the low-Ca pyroxene

376

377

378

379

380

381

382

383

384

385

386

387

host, is uncommon in mesosiderites. The investigated exsolution lamellae in pyroxene from mesosiderite A 09545 suggest, for this sample, a burial depth sufficient to guarantee the slow cooling rate or a reheating event with a peak temperature lower than 570°C, to allow the preservation of such delicate features. The simultaneous occurrence of the above described features in pyroxene points to the possibility that crystallographic investigations could define new mesosiderite subgroups, and ultimately new constraints on the thermal history and origin of the mesosiderite parent body.

Fig. 6.

Acknowledgements

The samples have been kindly provided by the National Institute of Polar Research, Tachikawa, Japan; the Royal Belgian Institute of Natural Sciences, Brussels, Belgium, and the Natural History Museum Vienna, Austria. The authors thank S. Van Den Broeck for the FIB cut at EMAT, Antwerp, Belgium, and F. Nestola and M. Murri for insightful discussions on the topic. LP is currently funded by the Austrian Science Fund (FWF). SMcK was supported by a Research Foundation - Flanders (FWO) postdoctoral fellowship (project 12O9515N) and is currently a postdoctoral fellow of the Alexander von Humboldt Foundation (project title: Early Solar System Pyroxenites). GJ was supported by the FWO project G.0603.10N. This research was funded by the BELAM project and the Interuniversity Attraction Poles Program Planet Topers, both financed by the Belgian Science Policy Office (BELSPO).

References

410 Agosto, W.N., Hewin, R.H., and Clarke Jr., R.S. (1980) Allan Hills A77219, the first
 411 Antarctic mesosiderite. *Geochimica et Cosmochimica Acta*, 14, 1027-1045.

412 Alvaro, M., Domeneghetti, M.C., Fioretti, A.M., Camara, F., and Minangeli, L. (2015) A
 413 new calibration to determine the closure temperatures of Fe-Mg ordering in augite from
 414 nakhlites. *Meteoritics and Planetary Science*, 50, 499-507.

415 Andraut, D., Pesce, G., Bouhifd, M.A., Bolfan-Casanova, N., Hénnot, J.M., and
 416 Mezouar, M. (2014) Melting of subducted basalt at the core-mantle boundary. *Science*,
 417 344, 892-895.

418 Ashworth, J.R. (1980) Chondrite thermal histories: Clues from electron microscopy of
 419 orthopyroxene. *Earth and Planetary Science Letters*, 46, 167-177.

420 Bogard, D.D., Garrison, D.H., Jordan, J. L., and Mittlefehldt, D. (1990) ^{39}Ar - ^{40}Ar dating
 421 of mesosiderites: Evidence for major parent body disruption < 4 Ga ago. *Geochimica et*
 422 *Cosmochimica Acta*, 54, 2549-2564.

423 Bogard, D.D. and Garrison, D.H. (1998) ^{39}Ar - ^{40}Ar ages and thermal history of
 424 mesosiderites. *Geochimica et Cosmochimica Acta*, 62, 1459-1468.

425 Brey, G.P. and Köhler, T. (1990) Geothermobarometry in Four-phase Lherzolites II.
 426 New thermobarometers, and practical assessment of existing thermobarometers. *Journal*
 427 *of Petrology*, 31, 1353-1378.

428 Brown, G.E., Prewitt, C.T., Papike, J.J., and Sueno, S. (1972) A comparison of the
 429 structures of low and high pigeonite. *Journal of Geophysical Research*, 77, 5778-5789.

430 Bunch, T.E. and Olsen, E. (1974) Restudy of pyroxene-pyroxene equilibration
 431 temperatures for ordinary chondrite meteorites. *Contributions to Mineralogy and*

432 Petrology, 43, 83-90.

433 Clayton, R.N., and Mayeda, T.K. (1996) Oxygen isotope studies of achondrites.

434 *Geochimica et Cosmochimica Acta*, 60, 1999-2017.

435 Delaney, J.S. (1981) Metamorphism in mesosiderites. *Proceedings of the 12th Lunar and*

436 *Planetary Science Conference*, p. 1315-1342.

437 Delaney, J.S. (1983) The formation of mesosiderites, pallasites, and other metal-silicate

438 assemblages: two mechanisms. *Meteoritics*, 18, 289-290.

439 Floran, R.J. (1978) Silicate petrography, classification, and origin of the mesosiderites:

440 review and new observations. *Proceedings of the 9th Lunar and Planetary Science*

441 *Conference* p. 1053-1081.

442 Ganguly, J., and Tirone, M. (2001) Relationship between cooling rate and cooling age of

443 mineral: theory and applications to meteorites. *Meteoritics and Planetary Science*, 36,

444 167-175.

445 Ganguly, J., Yang, H., and Ghose, S. (1994) Thermal history of mesosiderites:

446 Quantitative constraints from compositional zoning and Fe-Mg ordering in

447 orthopyroxenes. *Geochimica et Cosmochimica Acta*, 58, 2711-2723.

448 Goldstein, J.I., Yang, J., and Scott, E.R.D. (2014) Determining cooling rates of iron and

449 stony-iron meteorites from measurements of Ni and Co at kamacite-taenite interfaces.

450 *Geochimica et Cosmochimica Acta*, 140, 297-320.

451 Greenwood, R.C., Barrat, J.-A., Scott, E.R.D., Haack, H., Buchanan, P.C., Franchi, I.A.,

452 Yamaguchi, A., Johnson, D., Bevan, A.W.R., and Burbine, T.H. (2015) Geochemistry

453 and oxygen isotope composition of main-group pallasites and olivine-rich clasts in

454 mesosiderites: implications for the “Great Dunite Shortage” and HED-mesosiderite
 455 connection. *Geochimica et Cosmochimica Acta*, 169, 115-136.

456 Grove, T.L. (1982) Use of exsolution lamellae in lunar clinopyroxenes as cooling rate
 457 speedometers: an experimental calibration. *American Mineralogist*, 67, 251-268.

458 Haack, H., Scott, E.R.D., and Rasmussen, K. (1996) Thermal and shock history of
 459 mesosiderites and their large parent asteroid. *Geochimica et Cosmochimica Acta*, 60,
 460 2609-2619.

461 Haba, M.K., Yamaguchi, A., Kagi, H., Nagao, K., and Hidaka, H. (2017) Trace element
 462 composition and U-Pb age of zircons from Estherville: Constraints on the timing of the
 463 metal-silicate mixing event on the mesosiderite parent body. *Geochimica et*
 464 *Cosmochimica Acta*, 215, 76-91.

465 Hassanzadeh, J., Rubin, A. E., and Wasson, J.T., (1990) Compositions of large metal
 466 nodules in mesosiderites: links to iron meteorite group IIIAB and the origin of
 467 mesosiderite subgroups. *Geochimica et Cosmochimica Acta*, 54, 3197-3208.

468 Hewins, R.H. (1979) The pyroxene chemistry of four mesosiderites. *Proceedings of the*
 469 *10th Lunar and Planetary Science Conference*, p. 1109-1125.

470 Hewins, R.H. (1983) Impact versus internal origins for mesosiderites. *Proceedings of the*
 471 *14th Lunar and Planetary Conference. Journal of Geophysical Research*, 88, B257-B266.

472 Ishii, T., and Takeda, H. (1974) Inversion, decomposition and exsolution phenomena of
 473 terrestrial and extraterrestrial pigeonites. *Memoires of the Geological Society of Japan*,
 474 11, 19-36.

475 Lindsley, D.H. (1983) Pyroxene thermometry. *American Mineralogist*, 68, 477-493.

476 McCall, G.J.H. (1966) The petrology of the Mount Padbury mesosiderite and its
 477 achondrite enclaves. *Mineralogical Magazine*, 35, 1029-1060.

478 McCallum, I.S., Domeneghetti, M.C., Schwartz, J.M., Mullen, E.K., Zema, M., Camara,
 479 F., McCammon, C., and Ganguly, J. (2006) Cooling history of lunar Mg-suite
 480 gabbro-norite 76255, troctolite 76535 and Stillwater pyroxenite SC-936: The record in
 481 exsolution and ordering in pyroxenes. *Geochimica et Cosmochimica Acta*, 70, 6068-
 482 6078.

483 Miyamoto, M., and Takeda, H. (1977) Evaluation of a crust model of eucrites from the
 484 width of exsolved pyroxene. *Geochemical Journal*, 11, 161-169.

485 Miyamoto, M., Mikouchi, T., and Kaneda, K. (2001) Thermal history of the Ibitira
 486 noncumulate eucrite as inferred from pyroxene exsolution lamella: Evidence for
 487 reheating and rapid cooling. *Meteoritics and Planetary Science*, 36, 231-237.

488 Mittlefehldt, D.W. (1990) Petrogenesis of mesosiderites: I. Origin of mafic lithologies
 489 and comparison with basaltic achondrites. *Geochimica et Cosmochimica Acta*, 54, 1165-
 490 1173.

491 Mittlefehldt, D.W., McCoy, T.J., Goodrich, C.A., and Kracher, A. (1998) Non-chondritic
 492 meteorites from asteroidal bodies. In J.J. Papike Ed., *Planetary Materials*, pp. 4:1–4:195.
 493 Mineralogical Society of America, Washington D.C., USA.

494 Molin, G., Domeneghetti, M.C., Salviulo, G., Stimpfl, M., and Tribaudino, M. (2006)
 495 Antarctic FRO90011 lodranite: Cooling history from pyroxene crystal chemistry and
 496 microstructure. *Earth and Planetary Science Letters*, 128, 479-487.

497 Muir, I.D. (1954) Crystallization of pyroxenes in an iron-rich diabase from Minnesota.

498 Mineralogical Magazine, 30, 376-388.

499 Murri, M., Scandolo, L., Fioretti, A. M., Nestola, F., Domeneghetti, M.C., and Alvaro,
500 M. (2016) The role of Fe content on the Fe-Mg exchange reaction in augite. American
501 Mineralogist, 101, 2747-2750.

502 Nakamuta, Y., Urata, K., Shibata, Y., and Kuwahara, Y. (2017) Effect of NaCrSi₂O₆
503 component on Lindsley's pyroxene thermometer: an evaluation based on strongly
504 metamorphosed LL chondrites. Meteoritics and Planetary Science, 52, 511-521.

505 Nakazawa, H., and Hafner, S.S. (1977) Orientation relationship of augite exsolution
506 lamellae in pigeonite host. American Mineralogist, 62, 79-88.

507 Powell, B.N. (1969) Petrology and chemistry of mesosiderites: I. Textures and
508 composition of nickel-iron. Geochimica et Cosmochimica Acta, 33, 789-810.

509 Powell, B.N. (1971) Petrology and chemistry of mesosiderites-II: silicate textures and
510 compositions and metal-silicate relationships. Geochimica et Cosmochimica Acta, 35, 3-
511 34.

512 Pratesi, G., Moggi-Cecchi, V., Franchi, I.A., and Greenwood, R.C. (2009) NWA 4418:a
513 new mesosiderite from Northwest Africa. Proceedings of the 40th Lunar and Planetary
514 Science Conference, p. 2430.

515 Prior, G.T. (1918) On the mesosiderite-grahamite group of meteorites: with analyses of
516 Vaca Muerta, Hainholz, Simondium, and Powder Mill Creek. The Mineralogical
517 Magazine, 18, 151-172.

518 Putirka, K.D. (2008) Thermometers and Barometers for Volcanic Systems. In K. Putirka
519 and F. Tepley Eds., Minerals, Inclusions and Volcanic Processes, Reviews in Mineralogy

520 and Geochemistry, v. 69, pp. 61-120. Mineralogical Society of America, Washington
 521 D.C., USA.

522 Robinson, P., Ross, M., Nord Jr., G.L., Smyth, J.R., and Jaffe, H.W. (1977) Exsolution
 523 lamellae in augite and pigeonite: fossil indicators of lattice parameters at high
 524 temperature and pressure. *American Mineralogist*, 62, 857-873.

525 Rubin, A.E., and Jerde, E.A. (1987) Diverse eucritic pebbles in the Vaca Muerta
 526 mesosiderite. *Earth and Planetary Science Letters*, 84, 1-14.

527 Rubin, A.E., and Mittlefehldt, D.W. (1992) Classification of mafic clasts from
 528 mesosiderites: implications for endogenous igneous processes. *Geochimica et*
 529 *Cosmochimica Acta*, 56, 827-840.

530 Rubin, A.E., and Mittlefehldt, D.W. (1993) Evolutionary history of the mesosiderite
 531 asteroid: a chronologic and petrologic synthesis. *Icarus*, 101, 210-212.

532 Ruzicka, A., Boynton, W.V., and Ganguly, J. (1994) Olivine coronas, metamorphism,
 533 and the thermal history of the Morristown and Emery mesosiderites. *Geochimica et*
 534 *Cosmochimica Acta*, 58, 2725-2741.

535 Saxena, S.K. (1976) Two-pyroxene geothermometer: model with an approximate
 536 solution. *American Mineralogist*, 61, 643-652.

537 Saxena, S.K. (1983) Problems of the two-pyroxene geothermometry. *Earth and Planetary*
 538 *Science Letters*, 65, 382-388.

539 Scott, E.R.D., Haack, H., and Love, S.G. (2001) Formation of mesosiderites by
 540 fragmentation and reaccrction of a large differentiated asteroid. *Meteoritics and*
 541 *Planetary Science*, 36, 869-881.

542 Smith, J. V. (1969) Crystal structure and stability of the MgSiO₃ polymorphs; physical
 543 properties and phase relations of Mg-Fe pyroxenes. Mineralogical Society of America
 544 Special Papers, 2, 3-29.

545 Stadelmann, P. (2004) JEMS-EMS Java version, CIME-EPFL, CH-1015 Lausanne.
 546 <https://cime.epfl.ch/research/jems> (Visited on 8th January, 2019).

547 Stewart, B.W., Papanastassiou, D.A., and Wasserburg, G.J., (1994) Sm-Nd chronology
 548 and petrogenesis of mesosiderite. *Geochimica et Cosmochimica Acta*, 58, 3487-3509.

549 Stimpfl, M., Ganguly, J., and Molin, G., (2005) Kinetics of Fe²⁺-Mg order-disorder in
 550 orthopyroxene: experimental studies and applications to cooling rates of rocks.
 551 *Contributions to Mineralogy and Petrology*, 150, 319-334.

552 Sugiura, N., and Kimura, M. (2015) Reheating and cooling of mesosiderites.
 553 *Proceedings of the 46th Lunar and Planetary Conference*, p. 1646.

554 Tkalcec, B.J., Golabek, G.J., and Brenker, F.E. (2013) Solid-state plastic deformation in
 555 the dynamic interior of a differentiated asteroid. *Nature Geoscience*, 6, 93-97.

556 Ulmer, P., and Stalder, R. (2001) The Mg(Fe)SiO₃ orthoenstatite-clinoenstatite
 557 transitions at high pressures and temperatures determined by Raman-spectroscopy on
 558 quenched samples. *American Mineralogist*, 86, 1267-1274.

559 van der Hilst, R.D., and Karason, H. (1999) Compositional heterogeneity in the bottom
 560 1000 km of Earth's mantle: toward a hybrid convection model. *Science*, 283, 1885-1888.

561 Whitney, D.L., and Evans, B.W. (2010) Abbreviations for names of rock-forming
 562 minerals. *American Mineralogist*, 95, 185-187.

563 Wasson, J.T., and Hoppe, P. (2014) Co/Ni double ratios in mesosiderite metal and the
564 unrealistically low cooling rates. 77th Meteoritical Society Meeting, Abs. No. 5405.

565 Wasson, J.T., and Rubin, A.E. (1985) Formation of mesosiderites by low-velocity
566 impacts as a natural consequence of planet formation. *Nature*, 318, 168-170.

567 Yamaguchi, A., Taylor, G.J., and Keil, K. (1996) Global crustal metamorphism of the
568 Eucrite parent body. *Icarus*, 124, 97-112.

569 Yamaguchi, A., Pittarello, L., Kimura, M., and Kojima, H. (2014) Meteorite Newsletter
570 23. National Institute of Polar Research, Tokyo, Japan.

571 Yamamoto, J., Ishibashi, H., and Nishimura, K. (2017) Cooling rate responsiveness of
572 pyroxene geothermometry. *Geochemical Journal*, 51, 457-467.

573

Figure captions

Figure 1. Mesosiderite A 09545. **a)** Photo of the original meteorite. **b)** Thin section optical photo. **c)** BSE-SEM image mosaic.

Figure 2. First generation of exsolution lamellae in pyroxene from A 09545. **a)** BSE-SEM image of the mesosiderite, with the augite exsolutions with darker BSE contrast. **b)** Detail of lam 1 along cleavage. **c)** TEM image from the boundary between the host clinoenstatite (host px) and augite lam 1. **d)** Experimental zone-axis diffraction pattern (ZAP) of host (1) and lam 1 (2) and the corresponding simulated $[-7\ 0\ 12]$ and $[-14\ 0\ 27]$ ZAP respectively of clinoferrosilite (3) (similar to that of clinoenstatite) and augite (4).

Figure 3. Second generation of exsolution lamellae in pyroxene from A 09545. **a)** BSE-SEM image of pyroxene, with the augite exsolutions with darker BSE contrast and within them lam 2 with brighter contrast. **b)** TEM image from lam 1 with three sub-parallel lam 2. **c)** Detail from (b) showing the structural defects within lam 2. **d)** Experimental ZAP of lam 1 (1) and lam 2 (2) and the corresponding simulated $[-7\ 0\ 1]$ and $[6\ 0\ -1]$ ZAP respectively of augite (3) and clinoferrosilite (4).

Figure 4. Pyroxene composition diagram after Lindsley (1983). Data from this work and from literature (Estherville, Lowicz, Morristown, and Dyarrl Island after Hewins, 1979; Vaca Muerta and Patwar after Mittlefehldt et al. 1998).

Figure 5. Simplified pseudobinary pyroxene phase diagram for low pressure, after Muir, 1954, with the composition expressed as Wo content versus temperature. The path likely followed by pyroxene in A 09545 during slow cooling is marked with a dashed line. From the original melt composition (Wo_6), pigeonite (Pgt) crystallized. From Pgt

exsolved augite (Aug) formed upon cooling and with final compositions Wo_3 and Wo_{36} , respectively. From Aug, further exsolved low-Ca px (Wo_0) and the composition of Aug evolved to Wo_{42} . Finally, the original Pgt underwent transition from high to low and later to clinoenstatite. Mineral abbreviations according to Whitney and Evans (2010).

Figure 6. Simplified scenario for the formation of exsolution lamellae and the thermal evolution of A 09545. Compositions and temperatures after text and Table 1.

Table 1. Chemical composition of the pyroxene clasts and their lamellae as determined with the electron microprobe and TEM-EDS. The composition of the original exsolution lamellae and that of the recombined, bulk pigeonite precursor have been determined by relative percentages using image analysis. Composition is expressed in wt% oxides. Element content has been calculated as molar content. Standard deviation is given in brackets.

wt%	host px (avg #15)	lam 1 (avg #14)	lam1 (EDS) (avg #2)	lam 2 (EDS) (avg #2)	calculated composition lam1+lam2	calculated px original composition
SiO ₂	53.07(22)	52.56(34)	55	52	52.55	53.03
TiO ₂	0.44(3)	0.71(7)			0.61	0.46
Al ₂ O ₃	0.53(3)	0.97(12)			0.84	0.56
Cr ₂ O ₃	0.30(5)	0.48(4)			0.41	0.31
FeO	23.03(31)	10.37(64)	9	27	12.63	22.20
MnO	0.81(5)	0.48(6)			0.41	0.78
MgO	20.96(16)	14.39(24)	15	21	15.32	20.50
CaO	1.58(20)	20.36(49)	21	bdl	17.51	2.85
Na ₂ O	bdl	0.09(2)			0.08	0.02
K ₂ O	bdl	bdl			bdl	bdl
Total	100.72	100.41			100.37	100.71
Si	1.978	1.960	2.03	1.98	1.964	1.977
Ti	0.012	0.020			0.017	0.013
Al	0.021	0.043			0.037	0.025
Cr	0.009	0.014			0.012	0.009
Fe	0.718	0.323	0.28	0.86	0.395	0.692
Mn	0.026	0.015			0.013	0.025
Mg	1.165	0.800	0.83	1.19	0.853	1.139
Ca	0.063	0.813	0.83		0.701	0.114
Na	0.000	0.007			0.006	0.001
Tot	3.994	3.995	3.97	4.02	3.998	3.995
Wo	3	42	43	0	36	6
En	59	41	43	58	43	58
Fs	38	17	14	42	21	36
Mg#	62	71	75	58	68	62

Avq = average; bdl = below detection limit

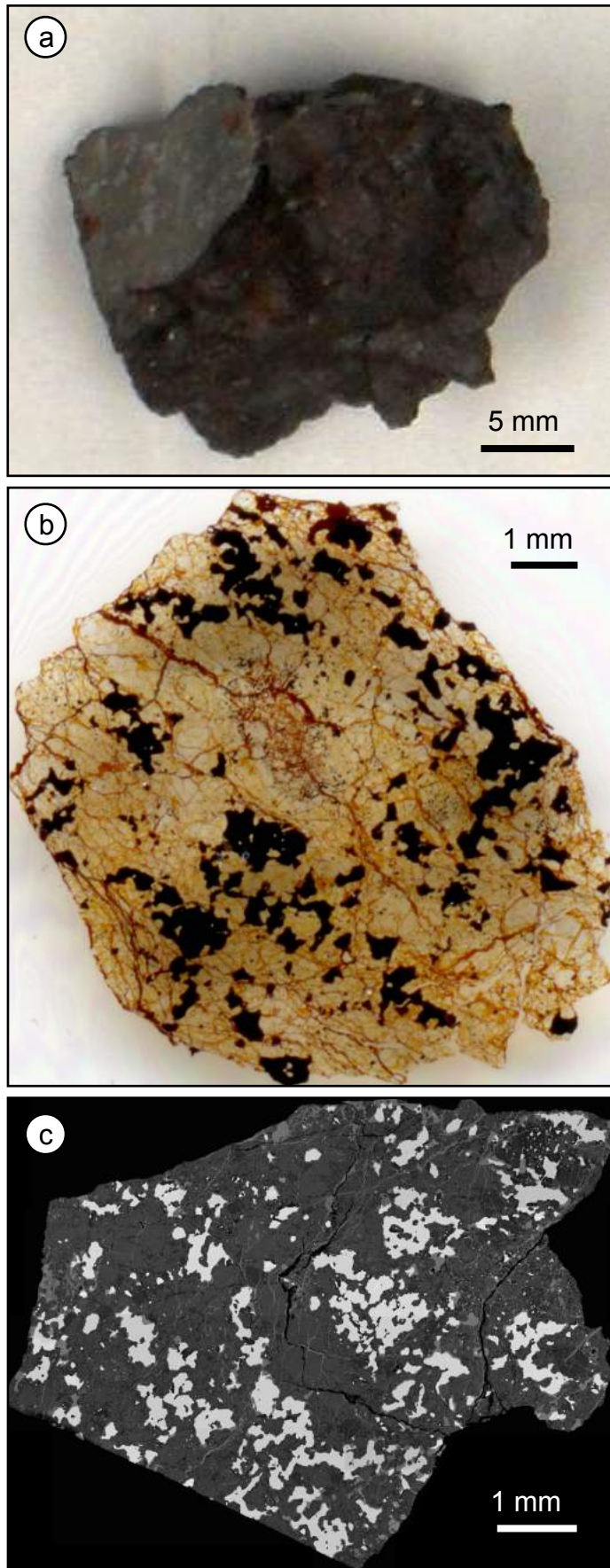


Fig. 1

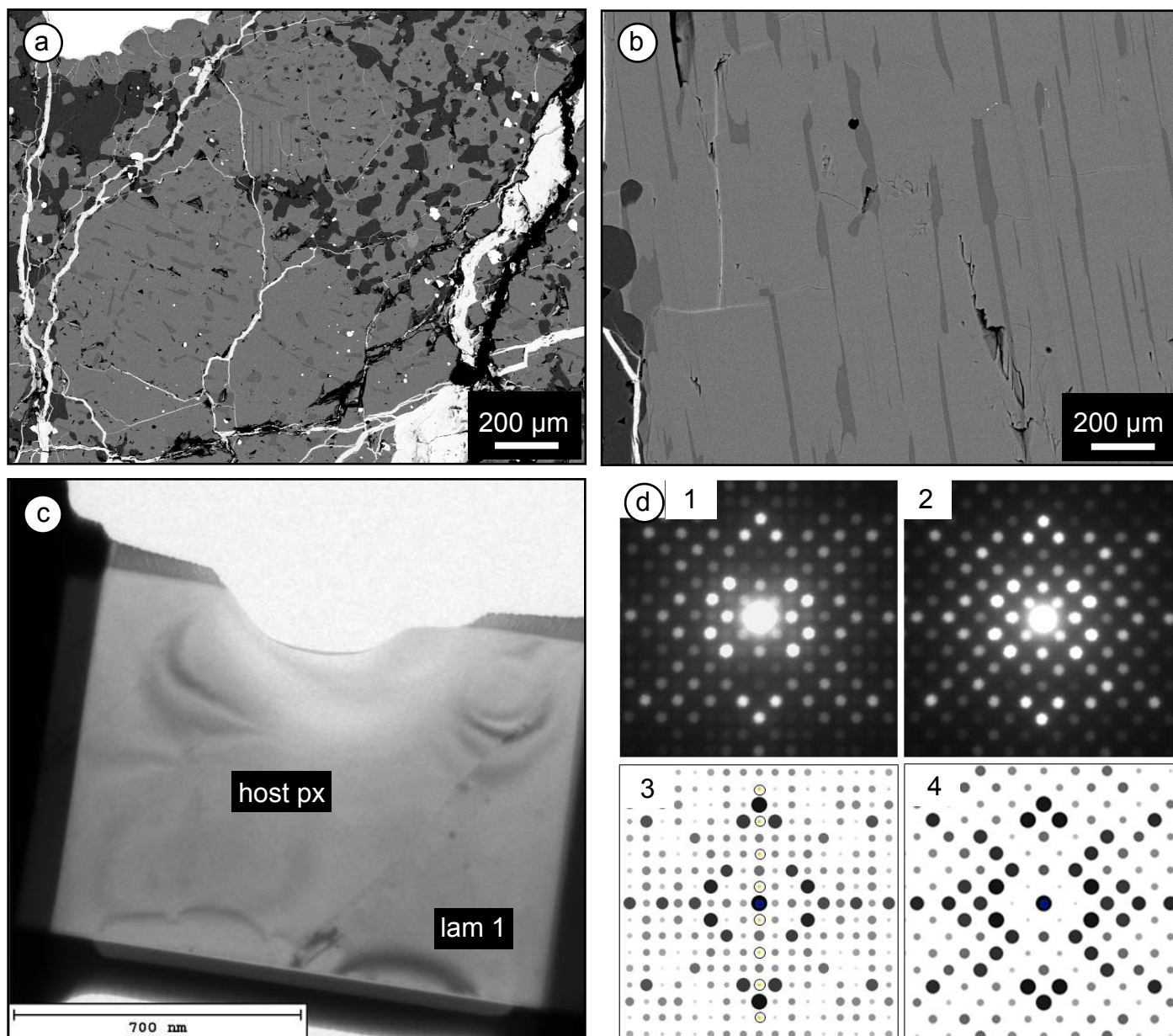


Fig. 2

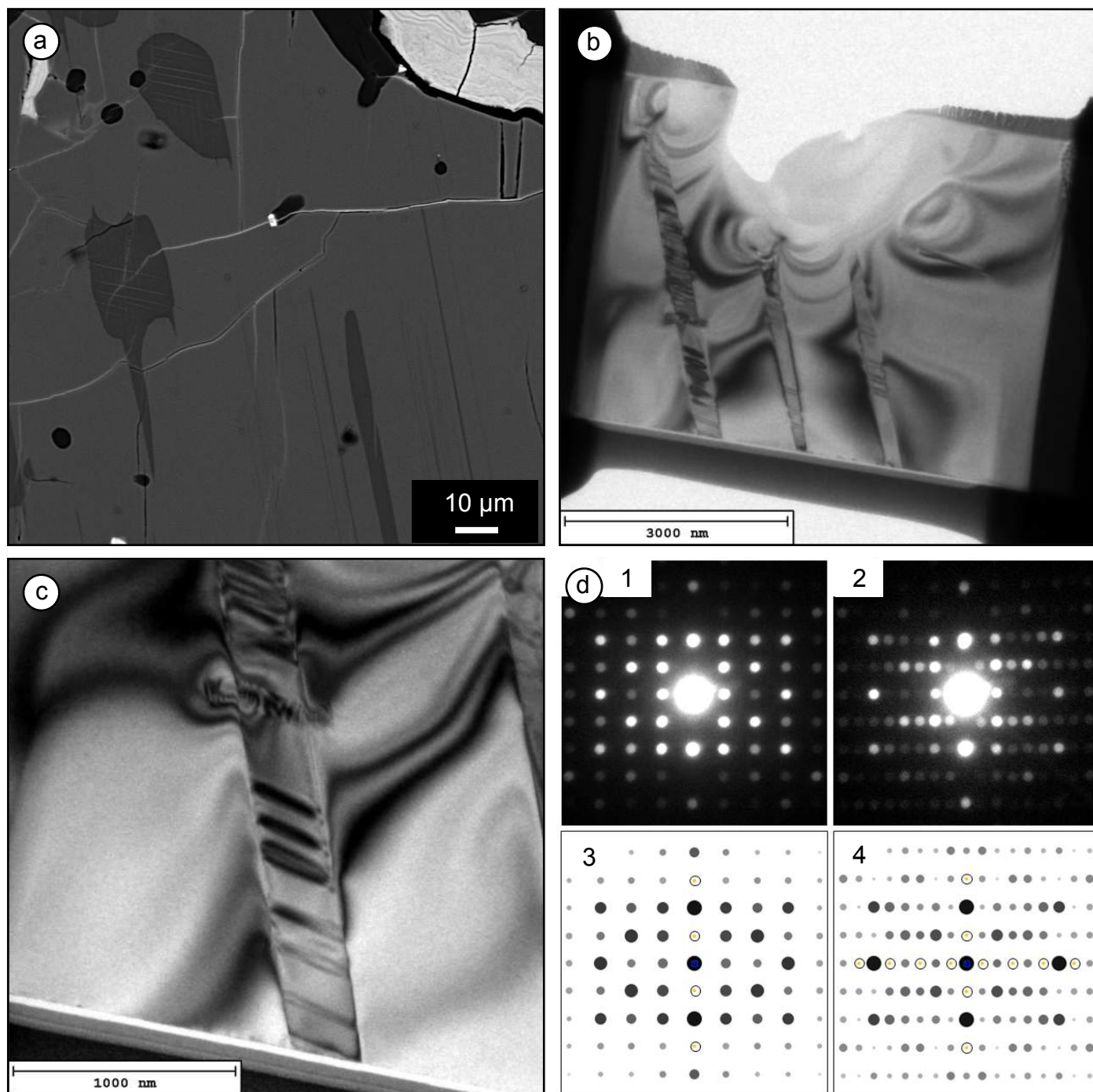


Fig. 3

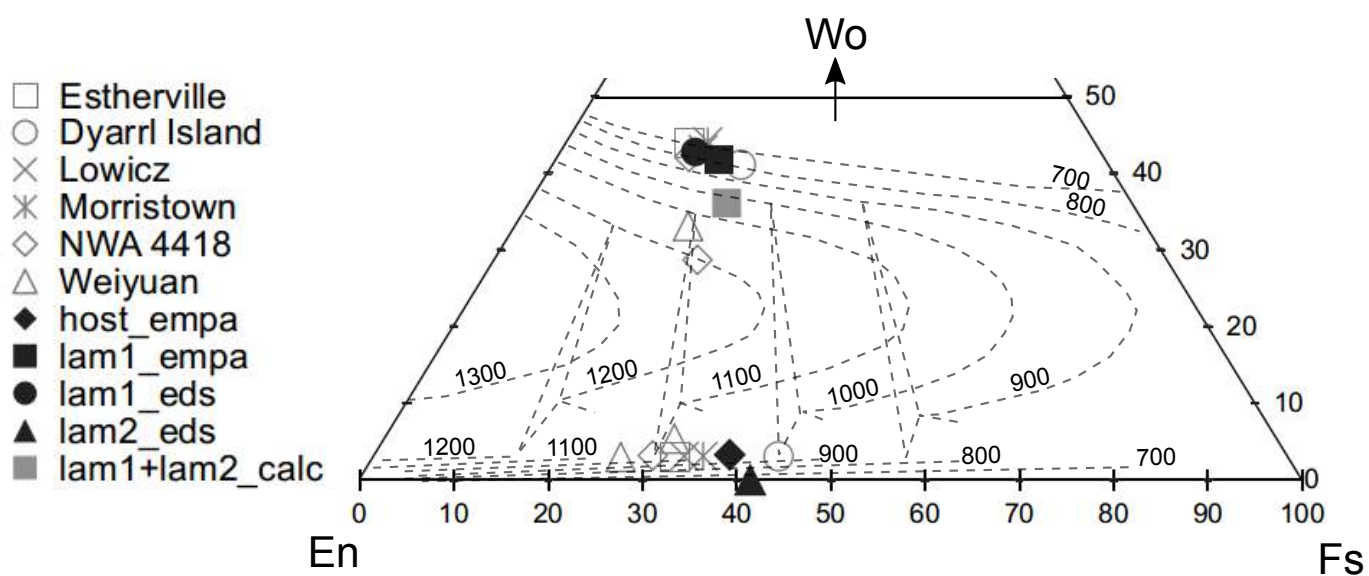


Fig. 4

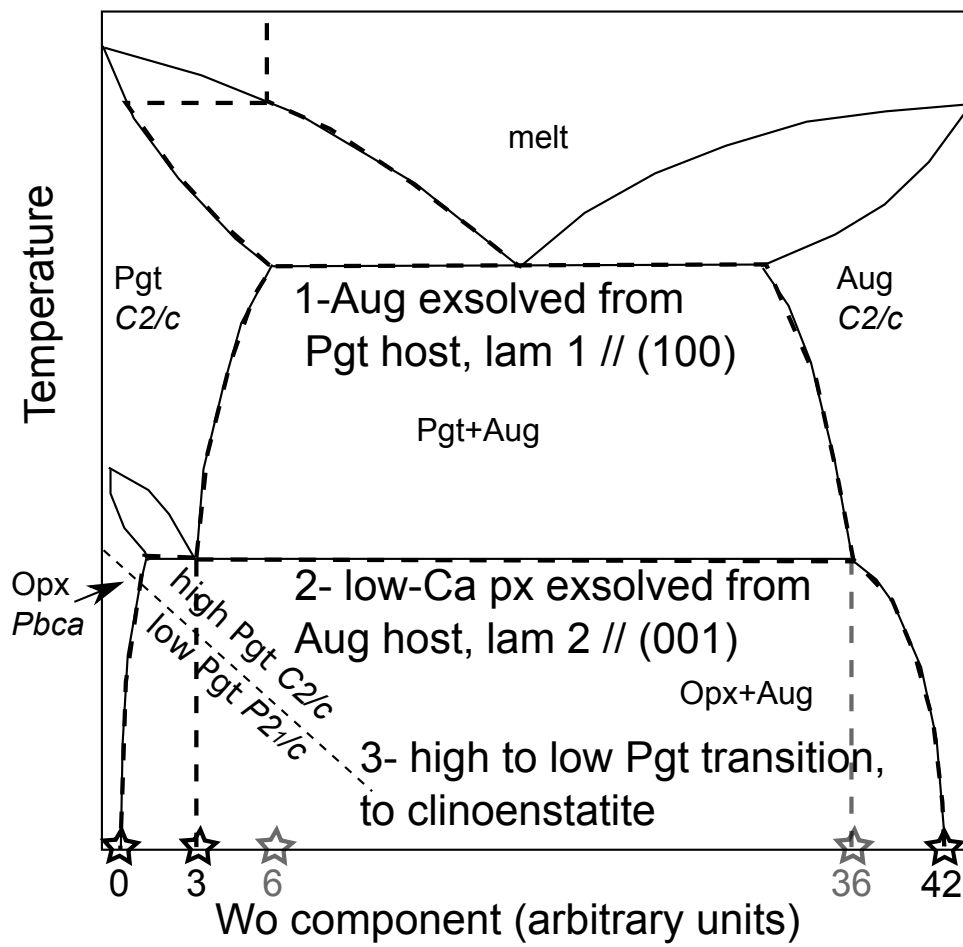


Fig. 5

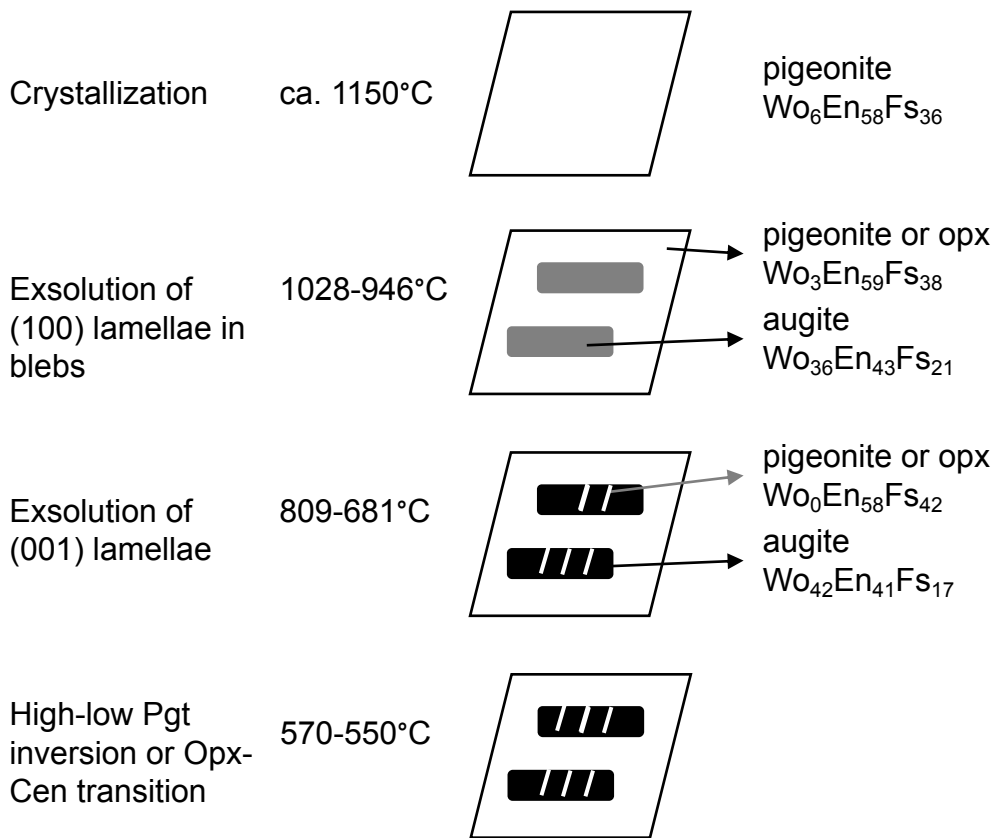


Fig. 6